Check for updates

ADVANCED FUNCTIONAL MATERIALS
www.afm-journal.de

Micro/Nanoarchitectonics of Ethanol-Unfolded Keratin for Dual-Function Biodegradable Nonwovens

Ruiyan Ni, Qiong Deng, Jiawen Zhang, Qinfei Ke, Chenchen Zhou, Nam-Joon Cho,* and Yi Zhao**

Nonwoven-based soilless cultivation holds promise for the cleanup of polluted brownfield areas, yet current substrates remain limited by single-functionality and inefficient pollutant removal. Existing surface-functionalized methods often require harsh pretreatment, toxic chemicals, or fall short in interfacial stability, thereby compromising material performance and biocompatibility. Here, a biodegradable Feather Keratin (FK)-functionalized planting geotextile is introduced through a simple and green ethanol-induced self-assembly process. Ethanol triggers FK molecular unfolding and promotes strong non-covalent adhesion onto jute and polylactic acid fibers, forming a uniform and robust coating without altering the underlying nonwoven structure. The resulting FK-functionalized nonwovens (FKNWs) exhibit a full transition to superhydrophilicity (water contact angle 121° to 0°), a 3.2 fold increase in liquid retention, and significant mechanical reinforcement (1.8 and 2 fold in the machine and cross directions). Furthermore, the FKNW delivers dual functionality by supporting vigorous plant growth and removing organic pollutants (43.5 mg g^{-1}) while retaining over 90% of protein loading and adsorption capacity after 20 flushing cycles. Owing to its straightforward fabrication, low cost, biodegradability, and integrated cultivation–remediation performance, FKNW represents a practical and scalable solution for the sustainable management and ecological restoration of contaminated brownfield sites.

1. Introduction

The emergence of brownfield sites in the cores of industrialized urban centers is increasing due to urban-planning constraints or land-use restrictions. It is estimated that there are more than 5 million of these potentially polluted brownfield sites globally.[1] Brownfield sites, often contaminated by industrial waste, hazardous substances, and decaying infrastructures, pose serious environmental and public health risks.[2,3] These sites are also associated with socioeconomic disadvantages in surrounding communities, including property devaluation and environmental injustice.[4,5] Therefore, the remediation and redevelopment of brownfield sites are imperative for supporting sustainable transition and improving urban ecosystem services. Although traditional remediation strategies can remove toxic chemicals, reclaim contaminated land for reuse, and mitigate urban sprawl, their net detrimental environmental impact may exceed that of inaction.[6]

Phytoremediation is an innovative, economical, and eco-friendly technology that relies on plants to remediate contaminants in soil or groundwater.[7] Among phytoremediation techniques, soilless cultivation offers an effective solution to soil-related limitations by minimizing the impact of soil-borne pollutants on early root growth and improving plant resilience to environmental stress during the critical seedling stage.[8] Nonwovens have attracted considerable attention in plant cultivation owing to their distinctive characteristics, including high porosity and air permeability, excellent mechanical properties, scalability, and robust water absorption and retention capabilities.[9] However, the bioremediation effect of plants is confined to the rhizosphere, making it challenging to remediate brownfield sites where contaminants

R. Ni, Q. Deng, J. Zhang, Y. Zhao
Shanghai Frontiers Science Center of Advanced Textiles
Donghua University
Shanghai 201620, China
E-mail: zhaoyi@dhu.edu.cn

R. Ni, Q. Deng, J. Zhang, Y. Zhao
Engineering Research Center of Technical Textiles
Ministry of Education
College of Textiles
Donghua University
Shanghai 201620, China

The ORCID identification number(s) for the author(s) of this article can be found under https://doi.org/10.1002/adfm.202530114

DOI: 10.1002/adfm.202530114

C. Zhou, N.-J. Cho
School of Materials Science and Engineering
Nanyang Technological University
Singapore 50 Nanyang Avenue, Singapore 639798, Singapore
E-mail: chenchen.zhou@ntu.edu.sg; njcho@ntu.edu.sg

C. Zhou, N.-J. Cho
Centre for Cross Economy
Nanyang Technological University
60 Nanyang Avenue, Singapore 637551, Singapore

Q. Ke
School of Perfume and Aroma Technology
Shanghai Institute of Technology
Shanghai 201418, China

 © 2026 Wiley-VCH GmbH

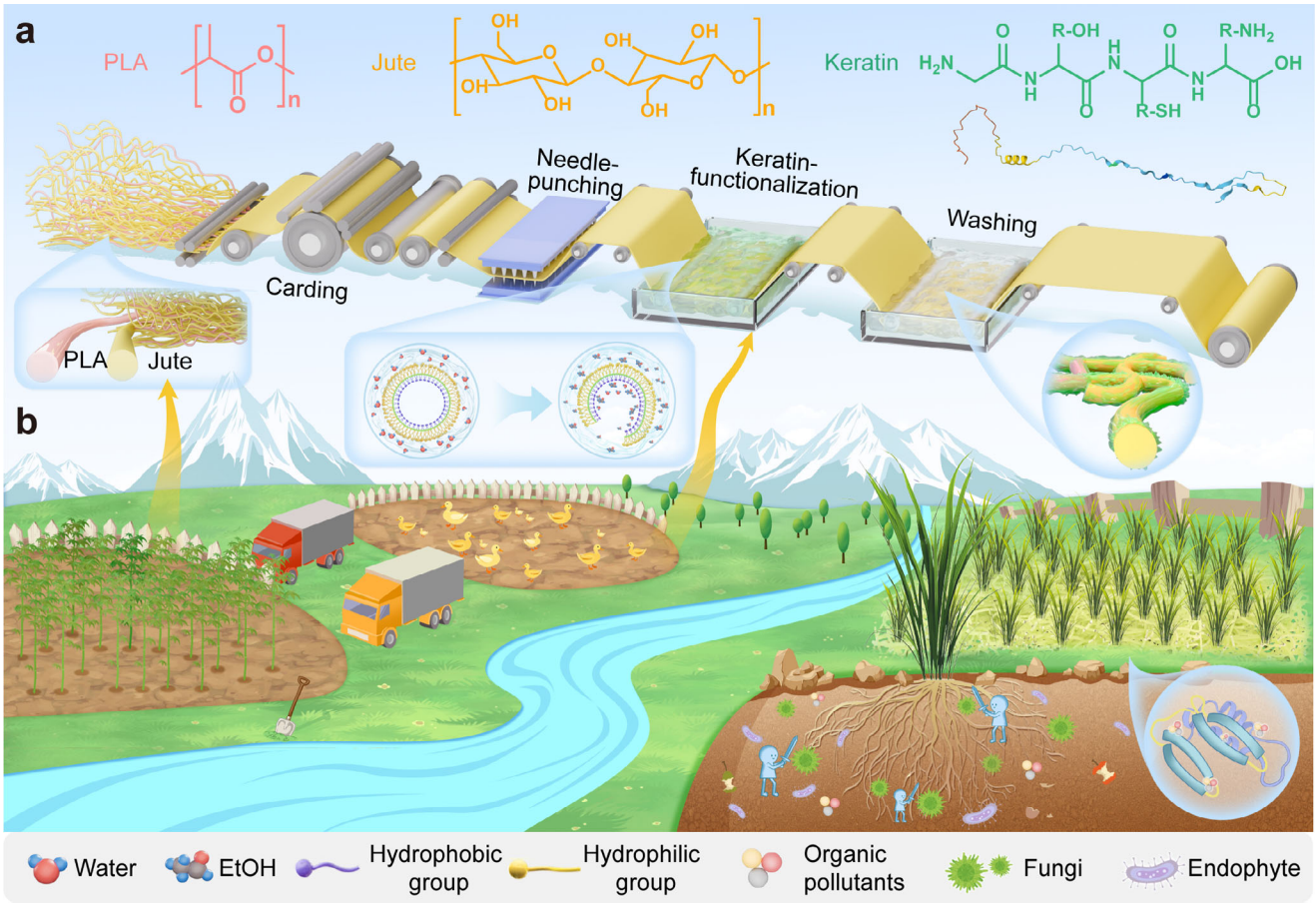

Figure 1. Fabrication and application of the feather keratin-functionalized nonwovens (FKNWs). a) Schematic illustration of the fabrication process of FKNWs, including fiber web formation, solidification, and keratin functionalization. b) Schematic showing the applications of FKNWs in plant cultivation and pollutant removal.

typically extend far beyond root zones. In addition, conventional nonwoven substrates are chemically inert and possess limited adsorption sites, resulting in single-functionality and insufficient pollutant removal capacity in complex environmental settings.

Nature has long served as a rich reservoir of valuable resources for developing functional materials and advancing sustainable technologies.[10–12] Feather keratin (FK) from livestock wastes, renowned for its biodegradability and unique macromolecular structure, exhibits universal molecular adhesion properties and a strong capacity to bind a wide range of contaminants in polluted environments.[13–16] Recent advances in keratin-based materials suggest that keratin exhibits surface-independent anchoring behavior via multiple molecular interactions, including van der Waals (VDW) forces, hydrophobic interactions, hydrogen bonding, and other attractive interactions. Liu et al.[17] successfully fabricated multifunctional keratin-functionalized polyamide 66 fabrics through the interaction with oxidized tannic acid, followed by metal ion chelation. The obtained coating formed a stable supramolecular network on the fabric surface through multiple interactions, comprising C—N and C—S bonds, π–π stacking, hydrophobic associations, coordination bonding, hydrogen bonding, and cation-π interactions. Lin et al.[18] employed keratin as a natural mediator to connect carbon nanotubes with poly(acrylamide) chains via hydrogen bonding, thereby improving the mechanical and electrical properties of strain sensors. Although these approaches effectively impart functions and improve materials' performance, they typically involve cumbersome pretreatment for different substrates and may undermine the intrinsic properties of the materials.

Herein, we propose a simple and scalable method to fabricate multifunctional planting geotextiles functionalized with FK through an ethanol-induced self-assembly strategy (**Figure 1a**). The addition of ethanol induces the unfolding of FK molecules and the exposure of domains, thereby promoting protein adhesion onto the needle-punched jute/polylactic acid (PLA) nonwovens (NWs) due to the multiple active sites are provided by the abundant polar and reactive groups on the FK peptide backbone. Meanwhile, ethanol lowers the surface tension of the solution and improves the wettability of the substrate, further promoting the adsorption of FK. A uniform and dense FK coating is ultimately formed on the fiber surface through a simple dipping process, without clogging the internal pores and sacrificing the inherent properties of pristine NWs. Furthermore, strong multiple non-covalent interactions between FK and fibers endow functionalized geotextiles with excellent water stability and durability under harsh conditions. Under the synergistic effect of the

© 2026 Wiley-VCH GmbH

16163028, 0, Downloaded from https://advanced.onlinelibrary.wiley.com/doi/10.1002/adfm.202530114 by Nanyang Technological University, Wiley Online Library on [11/01/2026]. See the Terms and Conditions (https://onlinelibrary.wiley.com/terms-and-conditions) on Wiley Online Library for rules of use; OA articles are governed by the applicable Creative Commons License

NWs and FK coating, the obtained FK-functionalized nonwovens (FKNWs) exhibit exceptional performance in both plant cultivation and pollutant adsorption (Figure 1b). This work demonstrates the feasibility of an ethanol-induced self-assembly strategy with FK as a building block to construct nanoarchitectonics on microarchitectonics nonwovens and imparting materials with enhanced wettability, liquid retention, mechanical property, and dual functions. This micro/nanoarchitectonics strategy not only offers a promising pathway for textile functionalization but also paves the way for the practical application of multifunctional nonwovens in real-world scenarios such as sustainable agriculture and environmental remediation.[19,20] Moreover, by transforming livestock-derived waste feathers and plant-based jute into high-value functional materials, this work exemplifies the principle of "treating waste with waste" and aligns with the cross-economy paradigm that promotes resource circularity, waste valorization, and carbon-neutral material solutions.[21]

2. Results and Discussion

2.1. Fabrication and Structural Characterization of FKNWs

The fabrication of FKNWs involves two simple steps (Figure 1a). First, fluffy NWs are fabricated by processing biodegradable jute and PLA fibers (Figure S1, Supporting Information) with a mass ratio of 7:3 using an industrial web-forming (carding) and consolidating (needle-punching) technique, which is fundamental for determining the physical and cultivation-related properties of the NWs. An ideal soilless cultivation substrate should possess sufficient mechanical strength to support plants while maintaining a favorable water–air environment, characterized by high air permeability and liquid absorption capacity. To optimize the NWs for plant growth, the effects of areal density, needle-punching depth, and needle-punching frequency on planting-related parameters are systematically investigated.

The tensile stress of NWs markedly increases with higher areal density due to enhanced fiber entanglement and improved load-bearing capacity, particularly in the machine direction (MD), rising from ≈0.5 MPa at 100 g m^{-2} to 1.7 MPa at 500 g m^{-2} (**Figure 2a**). The elongation at break in the MD remains relatively stable, while a slight decline (≈8.7%) is observed in the cross direction (CD) with increased areal density, possibly due to local stress concentration from excessive fiber stacking. Liquid absorption capacity improves progressively from ≈8.6 to 13.9 g g^{-1} as areal density increases, benefiting from enhanced capillary effects and smaller pore sizes resulting from the denser fiber matrix (Figure 2b). In contrast, air permeability decreases sharply from ≈3000 to 700 mm s^{-1}, indicating the increased airflow resistance due to denser fiber packing and reduced porosity. These results above indicate that lower areal densities offer better air permeability and promote root extension, while they exhibit insufficient mechanical robustness for root anchorage. Conversely, higher areal densities improve structural integrity and moisture retention but compromise airflow and increase costs. Therefore, 300 g m^{-2} is selected as the optimal areal density for subsequent experiments.

The tensile strength improves with the increment of needling depth, reaching a maximum of 1.3 MPa in MD and 0.4 MPa in CD at a depth of 11 mm due to the enhanced fiber entanglement (Figure 2c). However, a further increase in depth leads to a decline in strength due to fiber damage and structural weakening caused by excessive penetration. The elongation at break in MD remains scarcely influenced by variations in needling depth, maintaining ≈45–50%. In contrast, the elongation at break in CD exhibits a non-linear trend, initially decreasing and then increasing due to excessive compaction and network disruption, with the minimum value of 127% observed at 11 mm. A downward trend (≈17.6%) in water absorption is observed with increasing depth from 7 to 15 nm, potentially due to the reduced internal pore volume and limited water retention capacity. Nonetheless, the water absorption capacity exceeds 10 g g^{-1} across all depths (Figure 2d), demonstrating strong water retention capability. Meanwhile, air permeability decreases progressively from 1401 mm s^{-1} at 7 mm to 1119 mm s^{-1} at 15 mm, attributed to reduced porosity and densification of the fiber network. Despite reaching its lowest value at 15 mm, the air permeability remains above 1000 mm s^{-1}, which is sufficient to meet the aeration requirements of plant root systems. Overall, a needling depth of 11 mm offered the most favorable balance among mechanical strength, flexibility, air permeability, and liquid-adsorbing capacity, thus being selected as the optimal parameter for further processing.

The tensile strength initially improves with the increased needling frequency, reaching a maximum of 1.3 MPa in MD and 0.38 MPa in CD at 400 strokes min^{-1} due to the enhanced fiber entanglement (Figure 2e). However, further increases in frequency result in a decline in strength attributable to excessive fiber damage and structural weakening. Additionally, all samples exhibit favorable elongation properties, which are beneficial to facilitating robust root growth. The water absorption capacity gradually decreases from 12.7 to 9.1 g g^{-1} with increasing needling frequency (Figure 2f), attributed to reduced internal pore volume caused by the fiber densification. A similar trend is observed in air permeability, which declines from 1923 mm s^{-1} at 300 strokes min^{-1} to 1141 mm s^{-1} at 700 strokes min^{-1}. Notably, despite the decrease, the minimum air permeability remains above 1000 mm s^{-1}, which is adequate to satisfy the aeration requirements of plant root systems. Taken together, the NWs fabricated with a needling frequency of 400 strokes min^{-1} exhibit the most balanced and favorable performance.

Combined all results above, NWs fabricated with a areal density of 300 g m^{-2}, a needle-punching depth of 11 mm, and a frequency of 400 strokes min^{-1} are selected as the optimal substrate. Furthermore, a cultivation experiment was conducted to verify its feasibility as a planting geotextile. The ryegrass appeared lush and vibrant green after 15 days of growth, indicating that the NWs can provide a suitable environment for plant development (Figure S2, Supporting Information). Next, the prepared NWs are immersed in an ethanol-induced FK solution, followed by washing to obtain the FKNWs. Analysis of the effect of FK concentration on the loading and utilization rate (Figure S3, Supporting Information) shows that the loading rate increases with the concentration, from 11.2% at 0.5 wt% to 15.0% at 1 wt%. In contrast, the utilization rate reaches its highest value, 33.7% at 0.5 wt% and decreases as concentration increases. As a result, we chose a concentration of 0.75 wt% for the following study. FK molecules are firmly anchored onto the microscale fiber surface at this concentration, forming a continuous nanoscale coating with granular features (Figure 2g,h), which is further

© 2026 Wiley-VCH GmbH

16163028, 0, Downloaded from https://advanced.onlinelibrary.wiley.com/doi/10.1002/adfm.202530114 by Nanyang Technological University, Wiley Online Library on [11/01/2026]. See the Terms and Conditions (https://onlinelibrary.wiley.com/terms-and-conditions) on Wiley Online Library for rules of use; OA articles are governed by the applicable Creative Commons License

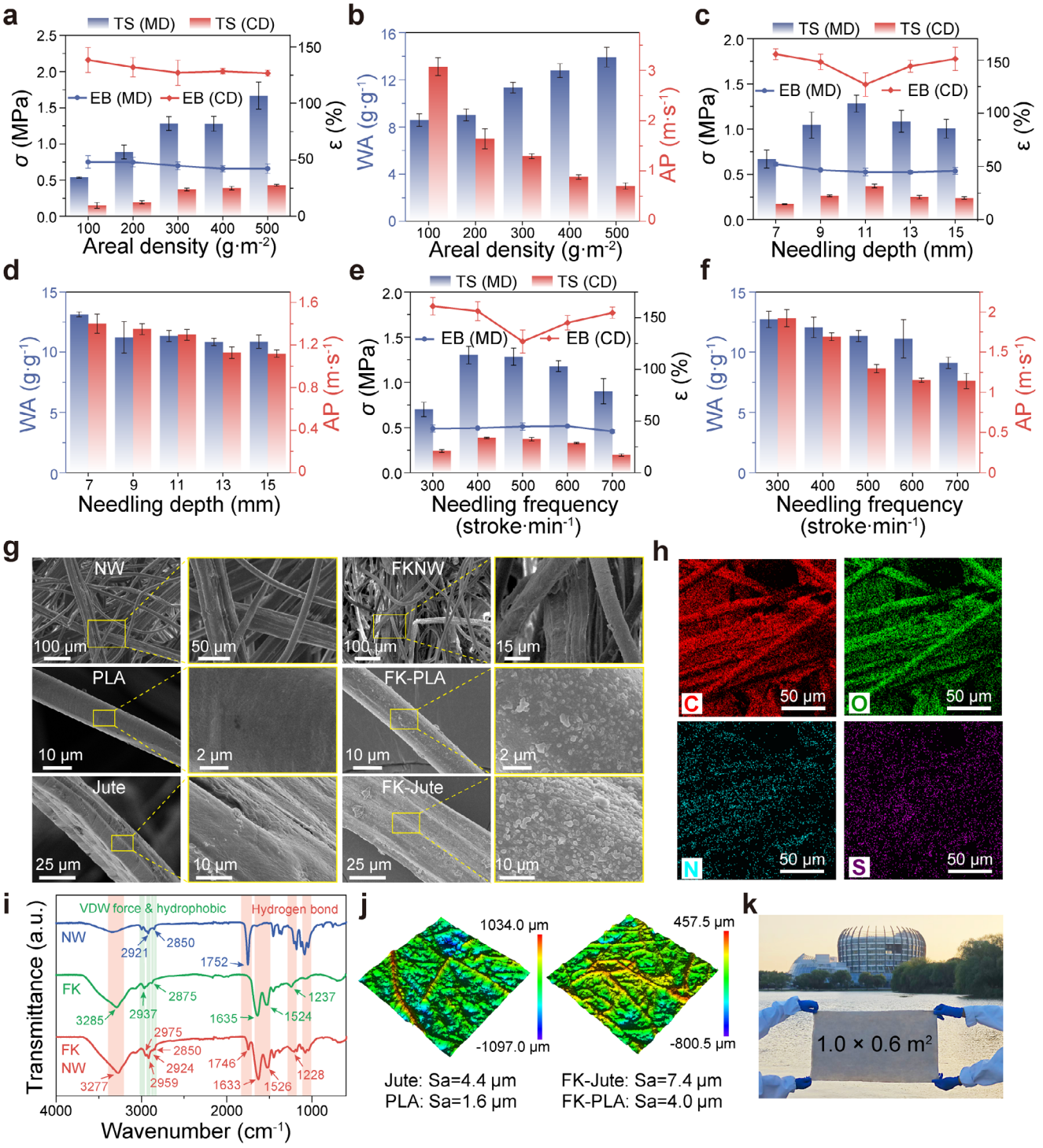

Figure 2. Fabricating optimization and characterizations of geotextiles. Tensile stress, elongation at break, water absorption (WA), and air permeability (AP) of jute/polylactic acid (PLA) nonwovens (NWs) with different (a, b) areal density, (c, d) needling depth, and (e, f) needling frequency. g) SEM images of jute/PLA NWs, PLA, and jute fiber before and after feather keratin (FK) functionalization. h) EDX mapping characterization of FKNW. i) FTIR spectra of NW, FK, and FKNW. j) 3D morphological images of NW (left) and FKNW (right). k) Photograph of a large-sized FKNW mat (length × width 1.0 × 0.6 m^2).

© 2026 Wiley-VCH GmbH

16163028, 0, Downloaded from https://advanced.onlinelibrary.wiley.com/doi/10.1002/adfm.202530114 by Nanyang Technological University, Wiley Online Library on [11/01/2026]. See the Terms and Conditions (https://onlinelibrary.wiley.com/terms-and-conditions) on Wiley Online Library for rules of use; OA articles are governed by the applicable Creative Commons License

confirmed by the appearance of new absorption peaks of the fourier transform infrared (FTIR) spectrum at 1633 cm^{-1} (amide I) and 1525 cm^{-1} (amide II) in FKNW (Figure 2i). Additionally, shifts of peaks from 3285 to 3277 cm^{-1} (the stretching vibration of O—H), 1524 to 1526 cm^{-1} (the stretching vibration of C—N), 1237 to 1228 cm^{-1} (the bending vibration of N—H), 1635 to 1633 cm^{-1} (the stretching vibration of C═O), and 1752 to 1746 cm^{-1} (the characteristic peak of ester group) confirm the existence of hydrogen bonding interactions between FK and the fiber surface.[22] Furthermore, the VDW force and hydrophobic interactions between FK and fiber are supported by the peak shift from 2921 to 2924 cm^{-1} and 2937 to 2959 cm^{-1} (the asymmetric stretching vibrations of C—H), and the decreased intensity of peaks at 2850 and 2875 cm^{-1} (the symmetric stretching vibrations of C—H).[16] Notably, the originally smooth surface of both jute and PLA fibers becomes markedly rougher after FK functionalization, with a roughness increasing from 4.4 to 7.4 µm and from 1.6 to 4.0 µm, respectively (Figure 2j). Furthermore, the successful fabrication of a large-sized FKNW mat (1.0 × 0.6 m^2) underscores the scalability of the process and highlights its great potential for functional nonwoven applications in soilless cultivation and environmental remediation (Figure 2k).

2.2. Mechanism Analysis of the Unfolding Behavior and Adsorption Process

During the self-assembly process, ethanol (EtOH) is employed to induce the unfolding of FK molecular chains and the exposure of domains by weakening or disrupting the non-covalent interactions that stabilize the native protein conformation. This unfolding behavior is confirmed by experimental results, including the increased average particle size from ≈8.8 to ≈26.13 nm, accompanied by a pronounced 10 fold enhancement in surface hydrophobicity and a marked shift in zeta potential from −14.6 to −4.2 mV (**Figure** 3a). FTIR deconvolution further reveals a pronounced transformation in secondary structure, with a substantial loss of β-sheet content from 62.6% to 40.2% and α-helix/random coil structures rising from 13.2% to 43.7% (Figure 3b,c). Molecular dynamics simulations are consistent with these findings, indicating the unfolding behavior and domains exposure of FK in DI/EtOH (Figure 3d) with the increased radius of gyration (Rg) and solvent-accessible surface area (SASA) (Figure 3e). Moreover, the ethanol-induced FK solution with lower surface tension overcomes the air/water interfacial barriers, allowing direct interaction between FK molecules and the surface of both hydrophobic PLA and hydrophilic jute fibers, respectively (Figure S4, Supporting Information). Ultimately, FK molecules are firmly anchored onto the microscale PLA and jute fiber surface, with a higher loading rate than the water-induced method (Figure 3a; Figure S5, Supporting Information).

Further, the adhesion of the FK coating to PLA and Jute is evaluated by nano-scratch testing (Figure 3f). Compared with the aqueous solution, the FK coating prepared via the ethanol-induced method exhibits superior adhesion to both PLA and jute, with adhesive forces increasing from 137 to 234 mN on PLA and from 211 to 236 mN on jute. Molecular dynamics simulations further reveal that ethanol-induced FK molecules undergo smaller conformational changes upon adsorption onto both hydrophobic PLA and hydrophilic jute fibers, as indicated by lower root-mean-square deviation (RMSD) (Figure 3g). This behavior is attributed to the pre-unfolded state of FK molecules in the ethanol environment, which facilitates more stable binding with fiber surfaces. Moreover, the total interaction energy of ethanol-induced strategy increases to 300 and 306 kJ mol^{-1} for PLA and jute, marking a 2.3 and 1.5 fold enhancement compared to the water-induced counterpart (Figure 3h). These findings indicate a strong adsorption affinity between FK molecules and both PLA and jute fiber surfaces, in agreement with the nano-scratch testing results. Such enhanced interactions contribute to tighter interfacial binding and improved conformational stability of the adsorbed FK molecules. In contrast, FK molecules in the aqueous system exhibit poor or unstable adsorption on the surface of both PLA and jute fibers (Figure 3i). Importantly, VDW force dominantly contributes to the total interaction energy, suggesting that the nonspecific physical interaction plays a critical role in the adsorption process. Given the inherently non-directional nature of the VDW force, the adsorption of FK onto fiber surfaces occurs without fixed orientation, resulting in a random molecular alignment during immobilization.[23] Upon subsequent volatilization of ethanol, a significant conformational rearrangement of the adsorbed FK coating is observed, characterized by an increase in β-sheet and β-turn content and a corresponding reduction in α-helix and random coil structures (Figure 3j,k; Figure S6, Supporting Information). This structural evolution underscores that ethanol not only facilitates the initial unfolding and surface anchoring of FK molecules but also governs the post-adsorption reorganization of molecular conformations, thereby acting as a dynamic regulator of protein self-assembly and structural stabilization at the fiber interface.

2.3. Various Property Tests and Comparisons of FKNW and NW

A favorable water-air environment is essential for plant growth in both indoor and outdoor conditions. The pristine NW is naturally hydrophobic with a water contact angle (WCA) as high as 121° (**Figure** 4a). After FK functionalization, the WCA rapidly decreases to 0° within 30 s, indicating a dramatic improvement in wettability. Such improved wettability is attributed to the synergistic effect of the intrinsic hydrophilic groups (–CONH–, –COOH, $–NH_2$, –OH) in the FK peptide backbone and the hierarchical structure of microscale fiber with nanoscale granular surface. This, in turn, contributes to the improved water absorption and retention capacity of FKNW, as evidenced by the higher liquid absorbing rate and a notably slower decline over time compared to NW throughout a 72 h period (Figure 4b). Correspondingly, visual observations show that FKNW retain moisture longer during drying, maintaining a visibly wetter state than NW at each time point (Figure 4c). After being left in the atmosphere for 48 h, the moisture content of FKNW is 2.5 times higher than that of the original NWs, highlighting its superior resistance to drought stress, which is an important factor in promoting plant growth.

Importantly, the FKNW exhibits negligible changes in pore size distribution (Figure 4d), porosity (Figure 4e), and air permeability, thereby preserving the key physical superiority of the original NWs. Moreover, a notable improvement in initial Young's

© 2026 Wiley-VCH GmbH

16163028, 0, Downloaded from https://advanced.onlinelibrary.wiley.com/doi/10.1002/adfm.202530114 by Nanyang Technological University, Wiley Online Library on [11/01/2026]. See the Terms and Conditions (https://onlinelibrary.wiley.com/terms-and-conditions) on Wiley Online Library for rules of use; OA articles are governed by the applicable Creative Commons License

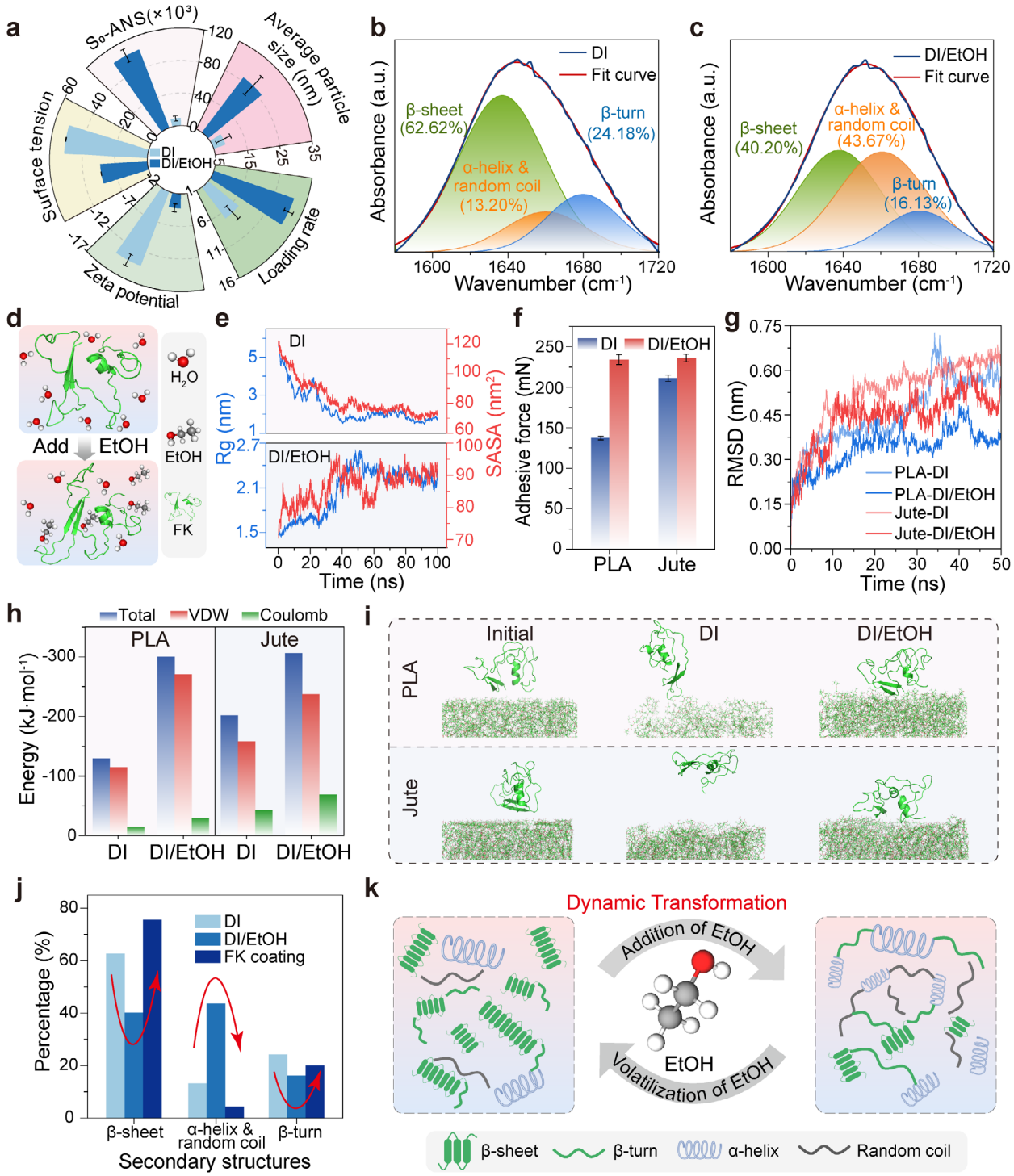

Figure 3. Mechanism analysis of ethanol (EtOH)-induced FK unfolding and adsorption process on the surfaces of PLA and jute. a) Surface tension, surface hydrophobicity (S_0-ANS), average particle size, zeta potential, and loading rate of keratin in DI and DI/EtOH solution systems (The surface hydrophobicity of FK is determined using 8-anilino-1-naphthalenesulfonic acid (ANS) as a fluorescent probe). Amide I region derived from FTIR spectrum deconvolution analysis of FK in b) DI and c) DI/EtOH solution systems. d) Molecular dynamics simulation reveals that FK undergoes unfolding in the presence of EtOH. e) The kinetic changes of keratin in radius of gyration (Rg) and solvent-accessible surface area (SASA) with the simulation time before and after ethanol-induced. f) Comparison of adhesive force of FK coatings induced by DI and DI/EtOH solutions with PLA and jute substrates. Comparison of g) root mean square deviation (RMSD) and h) total interaction energy for FK adsorbed onto PLA and jute fibers in DI and DI/EtOH systems. i) Molecular dynamics simulation diagrams illustrating the adsorption behavior of FK domains at the PLA and jute interfaces under the DI and DI/EtOH system after 50 ns. j) Proportion change of secondary structures of DI, DI/EtOH, and FK coating. k) Schematic diagram illustrating the "dynamic transformation" mechanism of EtOH on the secondary structure of keratin.

© 2026 Wiley-VCH GmbH

16163028, 0, Downloaded from https://advanced.onlinelibrary.wiley.com/doi/10.1002/adfm.202530114 by Nanyang Technological University, Wiley Online Library on [11/01/2026]. See the Terms and Conditions (https://onlinelibrary.wiley.com/terms-and-conditions) on Wiley Online Library for rules of use; OA articles are governed by the applicable Creative Commons License

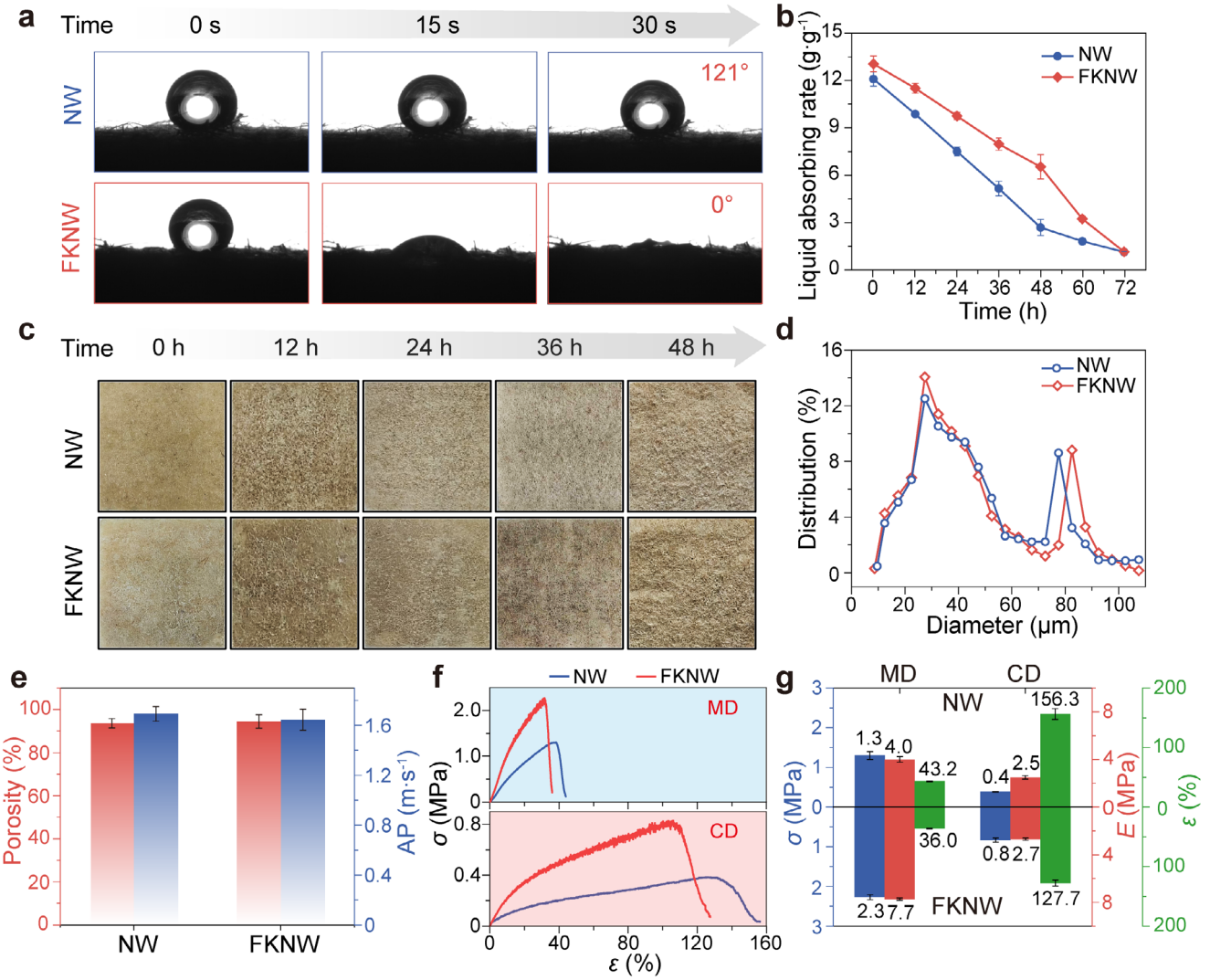

Figure 4. Performance tests and comparison between FKNW and NW. a) Dynamic wetting behavior of water droplets on NW and FKNW. b) Absorption liquid rate of NW and FKNW. c) Photographs of NW and FKNW after drying for different periods of time (12, 24, 36, and 48 h) under standard atmospheric conditions (a temperature of 20 ± 2 °C and relative humidity of 65 ± 4%). d) Pore size distribution, e) porosity, and air permeability (AP) of NW and FKNW. f) Stress–strain curves of NW and FKNW in the machine direction (MD) and cross direction (CD). g) Comparison of tensile stress (σ), initial modulus (E), and elongation break (ϵ) of NW and FKNW in MD and CD.

modulus and breaking strength in both MD and CD is observed, accompanied by a slight decline in elongation at break (Figure 4f,g). These phenomena are attributed to the formation of FK-based cross-linked network on the fiber surface, which enhances load transfer efficiency and reduces local stress concentration, while simultaneously restricting fiber slippage and deformation.

Conventional textile-functionalization approaches often suffer from a trade-off between introducing new functionalities and preserving the material's intrinsic properties. In contrast, the ethanol-induced self-assembly strategy employed in this work maintains the structural integrity and porous architecture of the original substrate, while simultaneously improving cultivation-related wettability, liquid retention capacity, and mechanical performance. Taken together, these advantages render FKNWs more favorable for supporting plant growth than pristine NWs, by sustaining an optimal water–air balance and improving surface microenvironment.

2.4. Dye Adsorption Analysis

Dye contaminants typically persist in brownfield sites due to historical industrial discharges, and their toxicity and resistance to degradation pose substantial risks to both ecosystems and human health.[1] FK exhibits the characteristics of "universal molecular adhesives" and outstanding capability in binding dye molecules owing to its abundant surface functional groups, such as hydroxyl, amino, carboxyl, and thiol groups.[24] Given this potential, Congo red (CR) is selected as a model pollutant to systematically assess and compare the adsorption performance of pristine NW and FKNW. The UV–vis absorbance of the dye

© 2026 Wiley-VCH GmbH

16163028, 0, Downloaded from https://advanced.onlinelibrary.wiley.com/doi/10.1002/adfm.202530114 by Nanyang Technological University, Wiley Online Library on [11/01/2026]. See the Terms and Conditions (https://onlinelibrary.wiley.com/terms-and-conditions) on Wiley Online Library for rules of use; OA articles are governed by the applicable Creative Commons License

solution significantly decreases after adsorption, indicating a substantial decrease in dye concentration (**Figure 5**a). The CR solution adsorbed by FKNW becomes nearly colorless, with a marked decrease in absorbance intensity from 0.42 to 0.03, whereas the NW-adsorbed solution shows only slight fading and retains a relatively high absorbance. The adsorption capacity (q_e) of FKNW reaches 43.48 mg g^{-1}, more than five times that of pristine NW (8.24 mg g^{-1}) (Figure S7, Supporting Information), demonstrating the remarkable improvement in dye removal performance achieved through FK functionalization.

The pH of the solution plays a crucial role in determining dye adsorption behavior by influencing the surface charge of the adsorbent, the ionization degree of dye molecules, and the interactions between them.[25] To explore this, the adsorption behavior of CR by FKNW is examined within a pH range of 5–9 (Figure 5b). The adsorption capacity decreases with increased pH. The maximum adsorption capacity (86.28 mg g^{-1}) observed at pH 5 can be attributed to the strong protonation of the FK surface group under acidic solution, which enhances electrostatic attraction with anionic dye molecules and further promotes adsorption.[26] Under alkaline conditions, reduced surface positive charge and the presence of competitive OH^- ions lead to a decline in adsorption capacity. Moreover, the adsorption isotherm and kinetics analysis reveal that the adsorption behavior fits well with the Langmuir isotherm equation and the pseudo-second-order kinetic model, indicating that the adsorption process is a monolayer surface coverage primarily dominated by chemisorption (Figure 5c–e; Tables S1 and S2, Supporting Information).

FTIR and X-ray photoelectron spectroscopy (XPS) analyses are performed on FKNW before and after adsorption. The FTIR spectra (Figure 5f,g) reveal multiple interactions and possible binding sites between FK and CR. The appearance of new peaks and shifts in characteristic absorption bands confirms the presence of molecular interactions. Specifically, the enhanced peak at 1179 cm^{-1} and the shifted peak at 1528 cm^{-1} correspond to the asymmetric stretching vibration of sulfonic acid groups and the stretching vibration of azo groups in CR, respectively.[27] In addition, the appearance of a new peak at 2997 cm^{-1} is attributed to the C—H vibration of the aromatic ring in CR. These spectral changes collectively confirm the successful adsorption of CR onto the FKNWs. Electrostatic interactions are verified by the enhancement of the peak at 1042 cm^{-1} (the symmetric stretching vibration of S═O) and the shift in the peak at 1633 cm^{-1} (the stretching vibration of C═O).[28] Hydrogen bond interactions between the molecular chains of FK and the CR are supported by the enhancement of peaks at 1213 cm^{-1} (the stretching vibration of C—N and bending vibration of N-H) and the shift of peaks at 3281 cm^{-1} (the stretching vibration of O—H and N—H). VDW interactions between the FK chains and benzene rings of CR are verified by the shifts at 2924 cm^{-1} (the asymmetric stretching vibration of CH_2 and CH_3), 2851 cm^{-1} (the symmetric stretching vibration of C-H) and 1633 cm^{-1} (the stretching vibration of aromatic C═C), which is associated to the aromatic ring vibration of CR. Additionally, hydrophobic interactions between the alkyl (-CH_3) groups in FK and CR are confirmed by the shift of the 2851 cm^{-1} peak (the symmetric C—H stretching vibration of -CH_3).[28]

Notably, an increase in the XPS S 2p peak at 164 eV is observed, with sulfur content rising from 0.68% to 1.34%, confirming the successful adsorption of CR onto the FKNW (Figure 5h). The high-resolution O 1s spectra reveal the characteristic peaks at 531.74 and 533.00 eV (Figure 5i), corresponding to the C—O—H and C═O groups, respectively. A new peak (S═O) at 534.4 eV further confirms the successful adsorption of CR. Additionally, the relative content of C—O—H decreases significantly from 70.02% to 36.90% after adsorption, indicating that the oxygen-containing functional group on the surface of the adsorbent may form a hydrogen bond with the highly electronegative oxygen and nitrogen atom of CR molecules.[29] The N—H peak at 400.00 eV shifts to 399.60 eV (Figure 5j) due to the hydrogen bond interaction between the -NH_2 group on FK and CR molecules.[30] Additionally, a new peak (-NH_3^+ group) appears at 401.86 eV after adsorption, attributed to the protonation of -NH_2 on FK, further suggesting that electrostatic attraction plays a key role in the adsorption process.[31] The C 1s spectra reveal that the content of C—N/C═N groups at ≈285.56 eV decreased from 41.82% to 30.31% after adsorption (Figure 5k), highlighting the involvement of amino groups during the adsorption process. Moreover, the slight shift of the C═O peak from 288.22 to 288.34 eV suggests the presence of π–π interactions between carbonyl groups in FK and the aromatic rings of CR. These results provide a comprehensive understanding of the molecular interactions involved in the dye adsorption process.

2.5. Performance Evaluation of FKNW in Plant Cultivation

To assess the impact of FK functionalization on plant cultivation, equal amounts of ryegrass seeds are uniformly sown on NW and FKNW. Both samples are irrigated with equal volumes of water, and plant height, root length, and water content are recorded periodically. Ryegrass cultivated on FKNW exhibits faster growth for both stem and root during the first 22 days than that on pristine NW (**Figure 6**a,b). Specifically, the plant height on FKNW reaches ≈80 mm by day 22, significantly surpassing the ≈55 mm observed for NW. Similarly, root length on FKNW extends to ≈60 mm by day 20, whereas NW only supports a root length of ≈43 mm. This enhanced early-stage growth can be attributed to the superior water retention capacity of FKNW, which better supports the water demands of ryegrass during the early stages of growth. After ≈30 days, both plant height and root length on both substrates become stabilized, likely indicating plant maturation.

Consistent with the observed trends in plant height and root length, the moisture content of ryegrass cultivated on FKNW is slightly higher than that on NW, particularly during the early growth stage (Figure 6c). The moisture content on FKNW increases rapidly over 80%, while that on NW lags behind at each time point, reaching only ≈75% by day 18. Subsequently, the moisture content in both substrates gradually approaches a plateau, converging ≈90% as the plants mature. The enhanced moisture uptake of FKNW is ascribed to the abundant active hydrophilic groups on FK, which facilitate the formation of hydrogen bonds with water molecules. As a result, FKNW provides a more stable and accessible moisture reservoir for plants, particularly in the critical early stage of growth. Photographic evidence further shows that both NW and FKNW substrates effectively support ryegrass growth (Figure 6d). Although ryegrass on FKNWs exhibits visibly denser and more vigorous growth compared to that on NWs, it reflects a more vigorous and healthier

© 2026 Wiley-VCH GmbH

16163028, 0, Downloaded from https://advanced.onlinelibrary.wiley.com/doi/10.1002/adfm.202530114 by Nanyang Technological University, Wiley Online Library on [11/01/2026]. See the Terms and Conditions (https://onlinelibrary.wiley.com/terms-and-conditions) on Wiley Online Library for rules of use; OA articles are governed by the applicable Creative Commons License

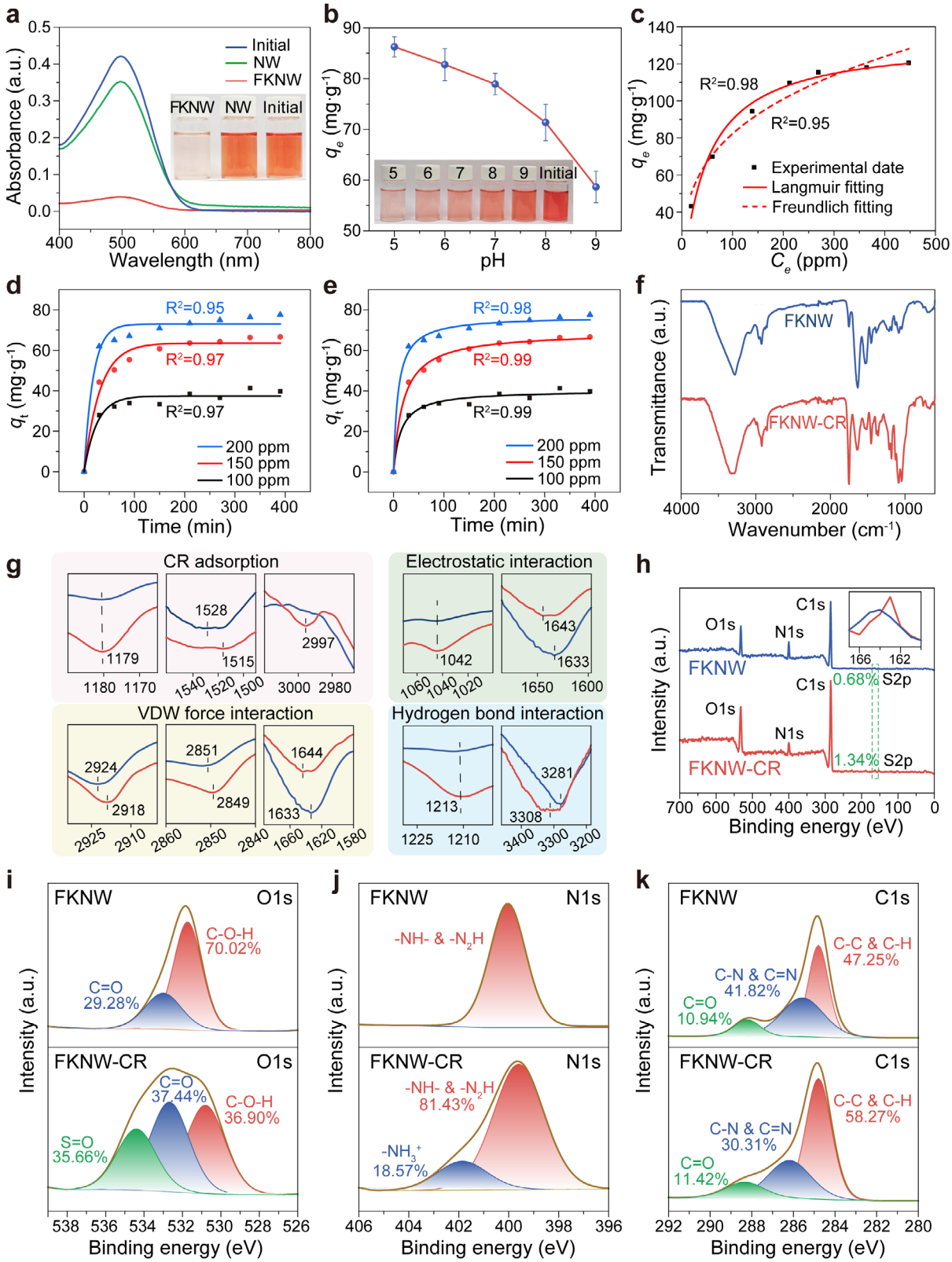

Figure 5. Adsorption behavior and interfacial interaction mechanism of FKNW for Congo red (CR). a) UV–vis spectra of the CR solution before and after NW and FKNW adsorption. b) Adsorption capacities of the FKNW for CR under varying pH. c) The adsorption isotherms curves of the FKNW. The adsorption kinetic curves of the FKNWs from d) pseudo-first order and e) pseudo-second order kinetic models. f, g) FTIR and h) XPS spectra of FKNW before and after adsorbing CR. High-resolution XPS spectra of i) O 1s, j) N 1s, and k) C 1s of FKNW before and after adsorbing CR.

© 2026 Wiley-VCH GmbH

16163028, 0, Downloaded from https://advanced.onlinelibrary.wiley.com/doi/10.1002/adfm.202530114 by Nanyang Technological University, Wiley Online Library on [11/01/2026]. See the Terms and Conditions (https://onlinelibrary.wiley.com/terms-and-conditions) on Wiley Online Library for rules of use; OA articles are governed by the applicable Creative Commons License

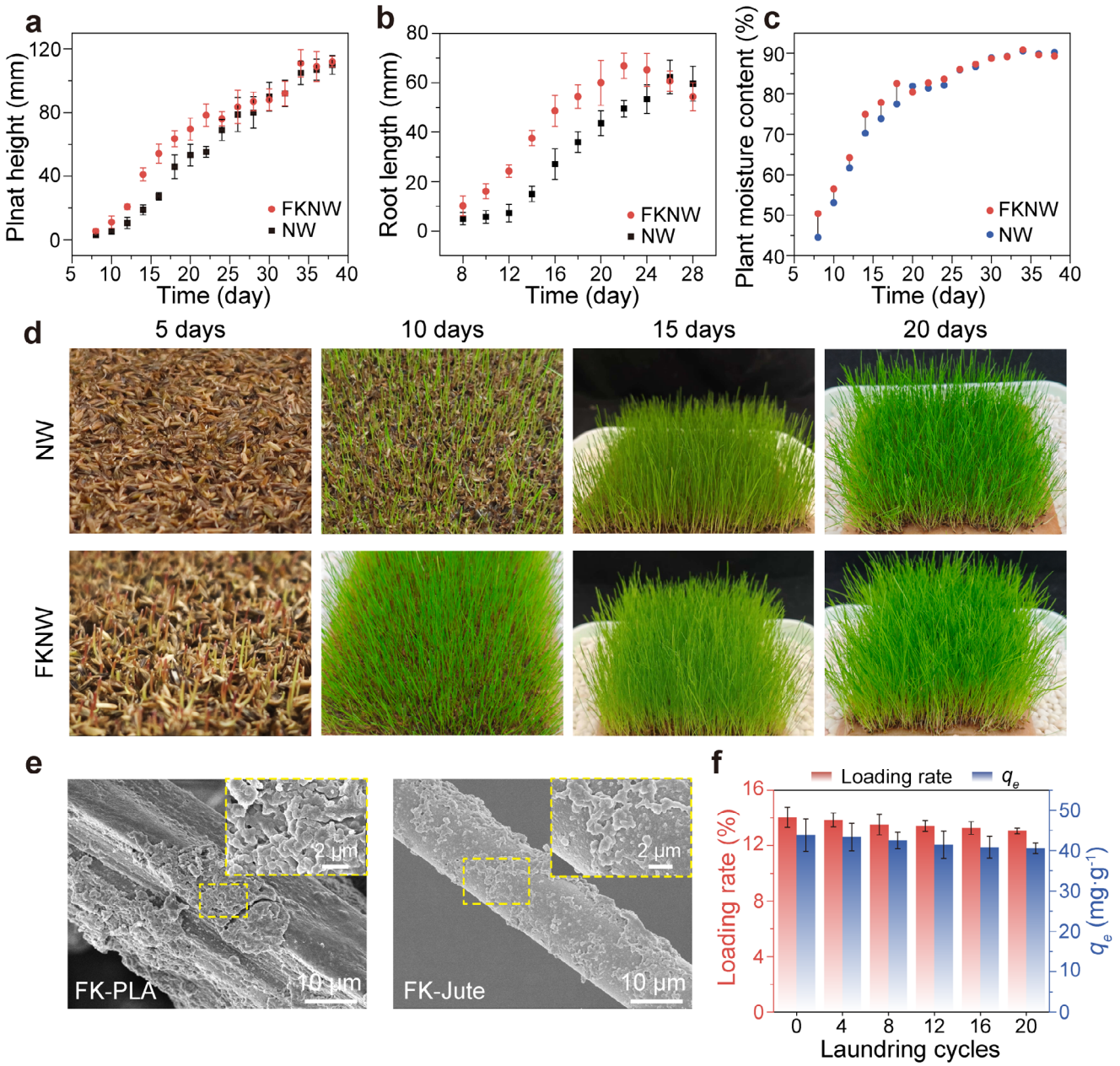

Figure 6. Growth of ryegrass on FKNW. a) Height, b) root length, c) moisture content, and d) photos of ryegrass plant on NW and FKNW. e) SEM images of FKNW after 20 rinsing cycles. f) Loading rate and adsorption capacity (q_e) variation of FKNW after 20 rinsing cycles. Data are presented as the mean ± s.d. (n = 3).

growth profile. This observation confirms that FK functionalization not only facilitates early-stage germination and development but also sustains robust plant growth over time, ultimately leading to enhanced biomass accumulation without disrupting the natural growth trajectory.

The adsorption and planting properties of FKNW are significantly improved after FK functionalization; however, the materials may be prone to the washing of surface runoff, such as rainwater, resulting in protein shedding in practical application scenarios. Cyclic flushing experiments are conducted to examine the interfacial stability of the FKNW. SEM images of FKNWs after 20 rinsing cycles clearly show that a substantial amount of FK still remains on both the PLA and jute fiber surfaces, with no obvious loss or peeling of the coating (Figure 6e). This indicates that the FK layer exhibits high water-stability and no detectable dissolution in practical use under the combined effects of disulfide crosslinking, enhanced surface hydrophobicity, and elevated β-sheet content.[32–36] Furthermore, the loading rate and q_e of FKNW for CR after 20 flushing cycles remain more than 90%, indicating that the FKNW is highly durable to the impact of water flow and has the potential for cyclic utilization (Figure 6f). SEM image comparisons between pristine FKNW and those after

© 2026 Wiley-VCH GmbH

16163028, 0, Downloaded from https://advanced.onlinelibrary.wiley.com/doi/10.1002/adfm.202530114 by Nanyang Technological University, Wiley Online Library on [11/01/2026]. See the Terms and Conditions (https://onlinelibrary.wiley.com/terms-and-conditions) on Wiley Online Library for rules of use; OA articles are governed by the applicable Creative Commons License

10 months of degradation reveal that pronounced surface roughness and erosion phenomena occurred on both jute and PLA fiber surfaces, along with the disruption and fragmentation of the FK coating, demonstrating that all three components have entered the degradation stage (Figure S8, Supporting Information). While a 10-month period is not sufficient to achieve full disintegration, these results clearly show that the FKNWs behave as biodegradable geotextiles and represent an environmentally benign alternative to conventional petroleum-based nonwovens.

3. Conclusion

In conclusion, a simple and effective ethanol-induced self-assembly strategy is developed to fabricate FK-functionalized planting geotextiles with integrated capabilities for pollutant adsorption and plant cultivation. The process enabled the uniform deposition of FK onto biodegradable jute/PLA NWs without blocking internal pores or sacrificing the intrinsic features of the pristine substrate. The resulting FK-functionalized geotextiles exhibit remarkably enhanced surface wettability (with the WCA reduced from 121° to 0°), a 3.2 fold increase in liquid retention capacity, and improved mechanical robustness by 1.8 and 2.0 times in MD and CD, respectively. This work highlights the potential of protein-based surface modification as a promising strategy for advancing sustainable materials in environmental remediation and ecological restoration. By transforming industrial waste, namely waste feather and jute, into biodegradable geotextiles for environmental remediation under the principle of "treating waste by waste", this work well exemplifies the concept of a cross-economy approach through a combination of materials innovation and sustainable process. Furthermore, this protein-based micro/nanoarchitectonics route, which combines the merits of both FK and nonwovens, is expected to extend traditional nonwovens into more advanced applications, including wastewater treatment, air filtration, bioactive wound dressing, and wearable healthcare textiles.

4. Experimental Section

Materials and Reagents: Jute, used as textile waste, was collected from a textile mill. PLA fiber was purchased from Shandong Three Thai Textile Co., Ltd., China. Duck feathers were supplied by Hangzhou Meiyu Clothing Co., Ltd, China. Cysteine (99.0%), urea (98.0%), sodium hydroxide (NaOH, 97.0%), and CR (99.0%) were purchased from Shanghai Aladdin Bio-Chem Technology Co., Ltd., China. Hydrochloric acid (HCl, 36.0-38.0%) was obtained from Sinopharm Chemical Reagent Co., Ltd., China. EtOH (99.7%) was supplied by Shanghai Titan Scientific Co., Ltd., China. Ryegrass seeds were purchased from Clover (Beijing) Eco-Tech Co., Ltd., China. All chemical reagents were of analytical grade or higher and used as received.

Extraction of Feather Keratin (FK): FK was extracted using the reduction preservation method according to our previous works.[37] First, duck feathers (30 g) were completely immersed in 300 mL of aqueous solution containing urea (8 M) and L-cysteine (10% based on the weight of the duck feather) at pH 10.5 and 70 °C for 12 h. The FK solution was centrifuged at 9000 rpm for 20 min to remove undissolved feather residues, followed by dialyzing against deionized water for 3 days. The purified FK solution was then stored at 4 °C for further use.

Fabrication of Nonwovens (NWs) and FK-Functionalized Nonwovens (FKNWs): NWs were fabricated through an industrial-scale web-forming (carding) and consolidating (needle punching) technique. Mixed fibers consisting of jute and PLA in a weight ratio of 7:3 were initially fed into a carding machine (Changshu Weicheng Co., Ltd., China) to produce uniform fiber webs. The webs, prepared with varying areal density, were subsequently overlapped and needle punched at different needling depths and frequencies to acquire NWs. NWs were directly immersed in a freshly prepared ethanol-induced FK solution (50% (v/v) of ethanol concentration). After immersing at room temperature for 24 h, the substrates were thoroughly washed with deionized water and dried to obtain FKNWs. The loading and utilization rate were calculated as per the following equations:

$$\text{Loading rate}\ (\%) = \frac{m_a - m_b}{m_b} \times 100\% \quad (1)$$

$$\text{Utilization rate}\ (\%) = \frac{m_a - m_b}{m_{fk}} \times 100\% \quad (2)$$

where "m_b" and "m_a" are the weights of NWs before and after FK-functionalization, respectively, and "m_{fk}" is the mass of FK.

Characterization: The pore size distribution of the materials was determined using a capillary flow porometer (PMI, CFP-1100AI, USA). The air permeability was measured with an automatic air permeability tester (YG461E, China). The contact angle and surface tension were evaluated using a contact angle measurement device (Dataphysics OCA15EC, Germany). Surface morphologies were observed by the field emission scanning electron microscope (FESEM, Hitachi S-8010, Japan) with an operating voltage of 5 kV. Surface roughness was measured using a 3D Measuring Laser Microscope (Olympus LEXT OLS5000, Japan). The chemical composition of the materials was analyzed by FTIR (Nicolet 6700, USA) and XPS(Escalab 250Xi, Thermo Fisher Scientific, USA). The adhesive force between the FK coating and fiber was measured by nano scratch testing (STEP500, Anton Paar, Austria) with a loading force range of 30 – 300 mN and a scratch velocity of 30 µm s^{-1}.

Areal Density and Porosity: Square specimens (side length a) were cut from each nonwoven and dried before testing. The total number n of specimens for each sample type was weighed, and their masses were recorded as m_1, m_2, ..., m_n. The areal density W (g m^{-2}) was calculated using the following equation:

$$W = \frac{m_1 + m_2 + \cdots + m_n}{n \times a^2} \quad (3)$$

where $a = 0.1$ m, n = 10. The porosity of the nonwoven is defined as the fraction of void volume to total volume, which can be calculated using the following formula:

$$\text{Porosity}\ (\%) = 1 - \frac{W}{t \times \rho} \times 100\% \quad (4)$$

where t (m) and ρ (g m^{-3}) represent the thickness and true density, respectively. The true density ρ was determined using a fully automated gas pycnometer (G-DenPyc 2900, Gold APP Instrument, China) based on the gas displacement method.

Mechanical Properties: The mechanical properties were measured using a multifunctional strength tester (YG026MB, Wenzhou Fangyuan Instrument Co., Ltd., China). Prior to the test, samples were cut into strips of 300 mm × 50 mm, and their thicknesses were measured by a thickness gauge (JC-YHD-2, China). A stretching speed of 100 mm min^{-1} and a gauge length of 50 mm were used throughout the experiments. Five replications were conducted for each sample, and the average values were used for analysis.

Water Absorption and Water Retention Capacity: The samples of known weights were immersed in distilled water for 24 h. Then, samples were weighed after removing excess water from the surface with a filter paper. The water absorbency (g g^{-1}) was calculated according to following equation:

$$\text{Water absorbency}\ \left(\text{g g}^{-1}\right) = \frac{W_{wet} - W_0}{W_0} \times 100\% \quad (5)$$

© 2026 Wiley-VCH GmbH

16163028, 0, Downloaded from https://advanced.onlinelibrary.wiley.com/doi/10.1002/adfm.202530114 by Nanyang Technological University, Wiley Online Library on [11/01/2026]. See the Terms and Conditions (https://onlinelibrary.wiley.com/terms-and-conditions) on Wiley Online Library for rules of use; OA articles are governed by the applicable Creative Commons License

where W_{wet} and W_0 are the weights of wet and dry samples, respectively. All experiments were carried out in triplicate. To assess water retention capacity, wet samples of known weight were transferred to a plastic mesh tray with a mesh hole of 2 mm × 2 mm under a temperature of 20 ± 2 °C and a relative humidity of 65 ± 4%. The sample was weighed and photographed at intervals of 12, 24, 36, 48, 60, and 72 h, and the water absorbency was calculated accordingly:

$$\text{Water retention}\ (\%) = \left(\frac{W_t}{W_{wet}}\right) \times 100\% \quad (6)$$

where W_t is the weight of retained water within the samples at time t. All experiments were carried out in triplicate.

Organic Dye Adsorption: Batch experiments were conducted to explore the adsorption efficiency of FKNWs for CR (as a model pollutant) by shaking a mixture of adsorbent (1 g) with dye solution (45 mL) at a certain concentration. The parameters of the adsorption experiment, including contact time (0–400 min), initial concentration (100–700 mg L^{-1}) and solution pH (5–9), were examined. The solution was filtered through a syringe with a 0.22 µm cellulose nitrate membrane filter after shaking for a predetermined duration. The initial and residual concentration of CR solution was monitored using a UV–vis spectrophotometer (UV–vis, TU-1901, China) at λ = 496.5 nm. The adsorption capacity ($Q_{t,e}$, mg g^{-1}) was calculated according to the following equation:

$$Q_{t,e} = \frac{(c_0 - c_{t,e}) \times v}{m} \quad (7)$$

where c_0 and $c_{t,e}$ (mg L^{-1}) are the initial and real-time or equilibrium concentrations of the solutions, m (g) denotes the mass of sorbent, and v (L) is the volume of solution. The adsorption kinetics and isotherms were further investigated to analyze the adsorption behavior of FKNWs toward CR.

Planting Experiment and Biodegradability Test: The washing stability of the FKNWs was evaluated by comparing the loading rate and adsorption capacity of the samples before and after washing. The washing process was performed at 25 °C with a shaking speed of 200 rpm for 6 h. After washing, the samples were removed and dried at room temperature prior to further analysis. The NWs and FKNWs were cut into a dimension of 200 mm × 200 mm. Equal amounts of ryegrass seeds were uniformly distributed on the surface of geotextiles and placed under identical environmental conditions. To facilitate optimal plant growth in the laboratory setting, 20 mL of water was poured daily. During the cultivation period, parameters such as plant height, root length, plant moisture content, and overall growth trends were monitored. Plants were also carefully taken out from the culture medium at designated time points. Surface moisture was removed using absorbent paper, and the fresh weight of the plants (M_0) was recorded. The fresh plants were subsequently dried in an oven to a constant weight to obtain the dry weight (M_1). The plant moisture content (%) was calculated by the following equation:

$$\text{Plant moisture content}\ (\%) = \frac{(M_0 - M_1)}{M_0} \times 100\% \quad (8)$$

The biodegradability of the FKNWs was evaluated by cutting them into small pieces of 10 × 10 cm^2 and burying them in natural soil at a depth of 2 cm. The sample was removed after being buried for 10 months from January to November 2025 for observation of its macroscopic and microscopic appearance to assess the biodegradability.

Molecular Dynamics Simulations: To investigate the structural changes of FK and its adsorption behavior on substrates under aqueous and ethanol solvent conditions, molecular dynamic simulations were conducted using the Gromacs 2022.5 open-source software package. All simulations were carried out in a closed system under periodic boundary conditions, with temperature and pressure maintained at 300 k and 1 bar, respectively. The sequence of FK (UniProt ID: P02450, KRFC_CHICK) was obtained from the Uniprot database. The molecular structure of ethanol was downloaded from the PubChem database and converted into 3D conformations using RDKit. RESP charges were calculated using ORCA 5.0 and Multiwfn 3.8, and GAFF-compatible force field parameters were generated using Sobtop 1.0. In the mixed solvent systems, ethanol–water mixtures were set at a volume ratio of 1:1. PLA and jute models were constructed using Packmol, and their RESP charges and GAFF topology files were obtained using the same manner as for ethanol. The protein was placed at the center of a cubic simulation box, ensuring a minimum distance of 1.0 nm between the protein and the box edge. The AMBERff99SB force field was used for the simulations, and the TIP3P model was employed for water molecules. Na^+ and Cl^- ions were added to neutralize the system. After constructing the initial system, energy minimization was performed using the steepest descent method. After fixing the protein positions, a 100 ps constant number of particles, volume, and temperature (NVT) equilibrium simulation was first performed, followed by a 100 ps constant number of particles, pressure, and temperature (NPT) equilibrium simulation. After NVT and NPT equilibration, both the wild-type and mutant systems were simulated for 100 ns with a simulation step of 2 fs. The bond lengths were constrained using a linear constraint solver, and long-range electrostatic interactions were calculated using the Particle Mesh Ewald method. A cutoff of 1.4 nm was used for both VDW and short-range Coulombic interactions. Upon completion of the simulations, structural analysis, including the calculation of the Rg and RMSD, was performed using the GROMACS gmx module.

Supporting Information

Supporting Information is available from the Wiley Online Library or from the author.

Acknowledgements

R.Y.N. and Q.D. contributed equally to this work. The authors gratefully acknowledge the financial support from the National Natural Science Foundation of China (Grant No. 22378057), the Donghua University 2025 Cultivation Project of Discipline Innovation (Grant No. xkcx-202515), the China Scholarship Council (Grant No. 202406630065), and the Fundamental Research Funds for the Central Universities and Graduate Student Innovation Fund of Donghua University (Grant No. CUSF-DH-D-2023021). This research was also supported by the Ministry of Education (MOE) in Singapore under the MOE AcRF Tier 3 grant (Grant No. MOE-MOET32022-0002) as well as the Korea Health Technology R&D Project through the Korea Health Industry Development Institute (KHIDI), funded by the Ministry of Health & Welfare, Republic of Korea (Grant No. HI22C1394) and Ministry of Agriculture, Food and Rural Affairs (Grant No. RS-2024-00403067).

Conflict of Interest

The authors declare the following competing financial interest(s): The work was submitted in patent disclosure.

Data Availability Statement

The data that support the findings of this study are available from the corresponding author upon reasonable request.

Keywords

ethanol-induced, feather keratin-functionalized, interfacial adhesion, molecular unfolding, nonwovens, plant cultivation, pollutants removal

Received: November 9, 2025
Revised: December 1, 2025
Published online:

© 2026 Wiley-VCH GmbH

16163028, 0, Downloaded from https://advanced.onlinelibrary.wiley.com/doi/10.1002/adfm.202530114 by Nanyang Technological University, Wiley Online Library on [11/01/2026]. See the Terms and Conditions (https://onlinelibrary.wiley.com/terms-and-conditions) on Wiley Online Library for rules of use; OA articles are governed by the applicable Creative Commons License

[1] D. Y. Hou, A. Al-Tabbaa, D. O'Connor, Q. Hu, Y.-G. Zhu, L. W. Wang, N. Kirkwood, Y. S. Ok, D. C. W. Tsang, N. S. Bolan, J. Rinklebe, *Nat. Rev. Earth Environ.* **2023**, *4*, 271.
[2] C. Mahammedi, L. Mahdjoubi, C. A. Booth, T. E. Butt, *Sci. Total Environ.* **2022**, *807*, 151069.
[3] Y. N. Song, N. Kirkwood, C. Maksimovic, X. D. Zheng, D. O'Connor, Y. L. Jin, D. Y. Hou, *Sci. Total Environ.* **2019**, *663*, 568.
[4] D. He, R. Zainol, N. S. Azali, *Ain Shams Eng. J.* **2024**, *15*, 103002.
[5] L. Loures, E. Vaz, *Habitat Int.* **2018**, *72*, 66.
[6] M. Owsianiak, G. Lemming, M. Z. Hauschild, P. L. Bjerg, *Environ. Sci. Technol.* **2013**, *47*, 1182.
[7] M. B. Kurade, Y.-H. Ha, J.-Q. Xiong, S. P. Govindwar, M. Jang, B.-H Jeon, *Chem. Eng. J.* **2021**, *415*, 129040.
[8] A. Kafle, A. Timilsina, A. Gautam, K. Adhikari, A. Bhattarai, N. Aryal, *Environ. Adv.* **2022**, *8*, 100203.
[9] W. Tan, L. Zhang, F. Fu, S. Bowman, P. Wang, Y. Y. Li, Y. Zhang, *J. Clean. Prod.* **2021**, *329*, 129788.
[10] C. C. Zhou, J. Y. Deng, J. H. Tay, S. Basu, J. Y. Yang, J. Li, C. M. Yang, Z. Zhao, N.-J. Cho, *Annu. Rev. Chem. Biomol. Engineer.* **2024**, *15*, 1.
[11] C. C. Zhou, S. S. Liang, B. Qi, C. X. Liu, N.-J. Cho, *Nat. Commun.* **2024**, *15*, 8862.
[12] L. Zhang, N. Ma, X. Z. Jia, T. J. Hua, J. Zhu, C. B. Ding, D. Z. Yang, J. R. Luo, M. L. Wang, J. J. Luo, S. Li, X. L. Tong, Q. Y. Fan, Z. Xia, Y. Y. Shao, M. Q. Jian, E. L. Gao, Y. L. Shao, J. Zhang, *Adv. Funct. Mater.* **2023**, *33*, 2301447.
[13] L. Faltova, A. M. Küffner, M. Hondele, K. Weis, P. Arosio, *ACS Nano* **2018**, *12*, 9991.
[14] R. Y. Ni, L. Zhang, J. J. Ma, J. W. Zhang, X. Y. Xu, H. Shi, Q. Deng, W. F. Hu, J. L. Hu, Q. F. Ke, Y. Zhao, *Nano Lett.* **2024**, *24*, 12891.
[15] Z. Y. Wang, N. Xiao, S. G. Guo, X. W. Liu, C. H. Liu, M. M. Ai, *J. Agric. Food Chem.* **2025**, *73*, 1014.
[16] B. S. Lazarus, C. Chadha, A. Velasco-Hogan, J. D. V. Barbosa, I. Jasiuk, M. A. Meyers, *Iscience* **2021**, *24*, 102798.
[17] L. N. Jiang, J. Y. Zhao, C. L. Zuo, W. Tan, Y. L. Ren, X. H. Liu, *Prog. Org. Coat.* **2024**, *197*, 108798.
[18] S. H. Zhu, Q. F. Zhou, J. Yi, Y. H. Xu, C. Y. Fan, C. X. Lin, J. Y. Wu, Y. Lin, *Adv. Sci.* **2023**, *10*, 2207400.
[19] J. W. Song, K. Kawakami, K. Ariga, *Adv. Colloid Interface Sci.* **2025**, *339*, 103420.
[20] K. Ariga, *Bull. Chem. Soc. Jpn.* **2024**, *97*, uoad001.
[21] N.-J. Cho, *Mater. Today* **2022**, *61*, 1.
[22] C. Vineis, I. Cruz Maya, S. Mowafi, A. Varesano, D. O. Sánchez Ramírez, M. Abou Taleb, C. Tonetti, V. Guarino, H. El-Sayed, *Int. J. Biol. Macromol.* **2021**, *190*, 375.
[23] F. Dismer, J. Hubbuch, *J. Chromatogr. A* **2007**, *1149*, 312.
[24] M. Peydayesh, R. Mezzenga, *Nat. Commun.* **2021**, *12*, 3248.
[25] L. Liu, Z. Y. Gao, X. P. Su, X. Chen, L. Jiang, J. M. Yao, *ACS Sustain. Chem. Eng.* **2015**, *3*, 432.
[26] U. A. Qureshi, Z. Khatri, F. Ahmed, M. Khatri, I.-S. Kim, *ACS Sustain. Chem. Eng.* **2017**, *5*, 4340.
[27] K. Z. Li, G. Q. Yuan, L. Dong, G. Deng, H. J. Duan, Q. L. Jia, H. J. Zhang, S. Zhang, *Sep. Purif. Technol.* **2022**, *302*, 122065.
[28] L. L. Deng, Y. Li, F. Q. Feng, H. Zhang, *Food Hydrocolloids* **2019**, *87*, 1.
[29] N. N. A. Malek, A. H. Jawad, A. S. Abdulhameed, K. Ismail, B. H. Hameed, *Int. J. Biol. Macromol.* **2020**, *146*, 530.
[30] C.-F. Wang, H. Liang, Z. Y. Song, J. C. Wu, Q. X. Li, *Int. J. Biol. Macromol.* **2025**, *308*, 142107.
[31] H. L. Liu, H. Yu, X. Yuan, W. J. Ding, Y. Li, J. K. Wang, *Chem. Eng. J.* **2019**, *374*, 1394.
[32] R. Floris, I. Bodnár, F. Weinbreck, A. C. Alting, *Int. Dairy J.* **2008**, *18*, 566.
[33] J. L. Kan, W. F. Li, R. Qing, F. Y. Gao, Y. M. Wang, L. C. Zhu, B. C. Wang, S. L. Hao, *Chem. Mat.* **2020**, *32*, 3122.
[34] H. M. Dai, F. C. Zhan, Y. J. Chen, Q. Shen, F. Geng, Z. Y Zhang, B. Li, *Int. J. Food Sci. Technol.* **2023**, *58*, 355.
[35] M.-J Tsai, Y.-M. Weng, *LWT* **2019**, *101*, 567.
[36] M. A. M. Mune, D. S. Sogi, S. R. Minka, *J. Food Process. Preserv.* **2018**, *42*, 13524.
[37] R. Y. Ni, M. R. Cheng, J. Meng, W. F. Hu, Q. F. Ke, Y. Zhao, *Int. J. Biol. Macromol.* **2023**, *238*, 124066.

© 2026 Wiley-VCH GmbH

16163028, 0, Downloaded from https://advanced.onlinelibrary.wiley.com/doi/10.1002/adfm.202530114 by Nanyang Technological University, Wiley Online Library on [11/01/2026]. See the Terms and Conditions (https://onlinelibrary.wiley.com/terms-and-conditions) on Wiley Online Library for rules of use; OA articles are governed by the applicable Creative Commons License